Relative impacts of permeability heterogeneity and viscosity contrast on solute mixing

A. Bonazzi,[1] M. Morvillo,[1] J. Im,[1] B. Jha,[2] and F. P. J. de Barros[1,*]

[1]*Sonny Astani Department of Civil & Environmental Engineering, University of Southern California, Los Angeles, California 90089, USA*

[2]*Mork Family Department of Chemical Engineering & Materials Science, University of Southern California, Los Angeles, California 90089, USA*

(Received 14 January 2021; accepted 28 May 2021; published 21 June 2021)

Solute transport in porous media is affected by several factors. The heterogeneous structure of the permeability field is a key factor controlling the spreading and mixing behaviors of a solute cloud. On the other hand, other factors such as the viscosity contrast between the dissolved solute and the ambient fluid can also play an important role. Although both these mixing mechanisms (field heterogeneity and viscosity contrast) have been acknowledged and studied, more investigations are needed in order to better characterize the effect of the variation of both the degree of viscous fingering and the level of disorder of the porous medium. This work aims to explore the impact of field heterogeneity and viscosity contrast on the transport behavior of an inert solute in a two-dimensional flow field. To achieve this, we performed high-resolution numerical simulations based on the spectral method to solve coupled flow and transport equations for a given range of viscosity contrast and log-permeability variance. We analyze the degree and rate of mixing, contour length of the solute cloud, spatial statistics of the concentration field, and arrival times at a control plane to characterize spreading and mixing in the domain. Through the use of numerical simulations, we provide a quantitative separation of the impacts of fingering and heterogeneity and we parametrize the concentration probability distribution function. We find that the interplay among viscous fingering, high-permeability channeling, and low-permeability stagnation at small scales create important features in the spreading and mixing characteristics. In particular, our results indicate that at early times viscosity contrast has a more significant impact on mixing than permeability heterogeneity, and the effect of viscosity contrast on early and late arrival times at a control plane is enhanced by increasing levels of permeability heterogeneity; on the other hand, heterogeneity reduces the peak concentration at a control plane and causes larger solute cloud spreading when the solute is more viscous than the ambient fluid compared to when the solute is less viscous. Moreover, we find that the concentration cumulative distribution function of the solute cloud can be described as a beta distribution for the range of viscosity contrast and permeability heterogeneity considered.

DOI: 10.1103/PhysRevFluids.6.064501

I. INTRODUCTION

The fundamental mechanisms controlling transport phenomena in natural porous formations are significantly affected by the spatially random fluctuations of the permeability field at different scales. The presence of heterogeneity in the permeability field leads to the creation of fast flow

*fbarros@usc.edu

channels that impact both the dispersive and mixing rate of the solute cloud [1–8] as well as first passage times [9–11]. These heterogeneity features have been investigated in applications such as management and remediation of groundwater contamination [12,13], artificial groundwater recharge [14], human health risk analysis [15,16], and CO_2 storage [17,18]. An often neglected but important aspect controlling transport is the viscosity contrast between the solute and the ambient fluid. As reported in the literature [19], groundwater contaminants such as nonhalogenated semivolatile compounds and jet fuel are more viscous than water. On the other hand, contaminants such as halogenated volatiles (amongst others) are less viscous than water. Moreover, the physical properties of a solute, such as viscosity, can vary in space and time due to the dependence of the property on the solute concentration and, therefore, mixing [20]. The contrast of viscosity between two fluids leads to the well-known phenomenon of viscous fingering, when the less viscous fluid displaces the more viscous fluid [21]. Viscous fingering is a type of hydrodynamic instability known as the Saffman-Taylor instability that occurs in porous media or Hele-Shaw cells under both miscible and immiscible flow conditions [22]. This phenomenon has received renewed attention due to its role in applications such as enhanced oil recovery [20,23], geological CO_2 storage [24], and chromatography separation [25].

The effect of viscous fingering on spreading and mixing of fluid slugs has been reported through laboratory experiments and numerical simulations. Experiments have been conducted using Hele-Shaw cells [26,27], glass beads or sand packs [28–30], and naturally consolidated rocks [31,32]. Numerical simulations have been conducted using higher-order finite difference methods [33,34], particle tracking methods [35], spectral methods [36–39], and compact finite difference–finite volume methods [20,40–42]. The effect of low levels of heterogeneity on spreading of slugs due to viscous fingering has also been studied [32,40,43–50]. Nicolaides *et al.* [19] showed how the interplay between two sources of disorder (i.e., viscosity contrast and physical heterogeneity of the porous medium) impacted macroscopic features of the solute transport behavior, namely solute breakthrough and removal times and mixing, in a flow field induced by injection and extraction wells.

Our work focuses on further understanding of the joint role of medium heterogeneity and viscous fingering on solute transport under miscible flow conditions. The analysis carried out in the present contribution differs from Nicolaides *et al.* [19] by considering additional mixing and statistical metrics such as the concentration statistical distribution. Differently from the work of Nicolaides *et al.* [19], we consider transport under uniform-in-the-mean flow conditions. Our flow configuration mimics an ambient flow, while in Nicolaides *et al.* [19] the flow is controlled by injection and extraction wells. The presence of wells in the flow field impact the solute's mixing behavior and its concentration statistics (see [51]). We are particularly interested in quantifying the *relative importance* of the two factors in the overall transport behavior. We achieve this goal in two ways. First, we provide a theoretical analysis of how the sources of disorder, namely viscosity contrast and medium heterogeneity, affect the solute transport process. Second, through the use of high-resolution numerical simulations, we examine the effects of both medium heterogeneity and viscosity contrast on the temporal evolution of statistical descriptors of transport (i.e., concentration mean, variance, and probability density function) and the solute cloud's contour length. These metrics provide important information about the solute mixing state [52], and therefore its eventual chemical reactivity [6,53], and assist site managers to estimate the risks associated with contamination [54]. For example, the effectiveness of groundwater remediation techniques may be related to the contact surface area between two fluids, which is increased by solute spreading [55,56]. We also show how the early breakthrough, associated with the leading edge of the solute cloud, is impacted by permeability heterogeneity and viscous fingering. Differently from previous works, we introduce two metrics that provide a quantitative separation of the impacts of fingering and heterogeneity. These two metrics allow one to characterize and clarify the interplay between heterogeneity and viscosity contrast on the macroscopic transport behavior. Finally, a relation between the solute cloud's concentration cumulative distribution function (CDF) and the beta distribution is reported.

II. THEORETICAL BACKGROUND

A. Governing equations

In this work, we consider a two-dimensional (2D) porous medium where $\mathbf{x} = (x_1, x_2)$ is the Cartesian coordinate system. The physical domain has dimensions $L_1 \times L_2 = \{(x_1, x_2)|x_1 \in L_1 \text{ and } x_2 \in L_2\}$. The permeability of the porous medium, denoted by $k(\mathbf{x})$, is assumed to be locally isotropic and spatially heterogeneous. Furthermore, we assume a constant porosity ϕ. The spatially heterogeneous structure of the log-permeability $f(\mathbf{x}) \equiv \ln[k(\mathbf{x})]$ is considered to be multi-Gaussian and modeled through a random space function (RSF) [57]. The RSF model for f is characterized by its mean $\langle f \rangle$, variance σ_f^2, and a correlation length λ. The angled brackets $\langle \cdot \rangle$ represent the average operator. In this study, we adopt an isotropic Gaussian log-permeability covariance model:

$$\mathcal{C}_f(\mathbf{r}) = \sigma_f^2 e^{-\mathbf{r}^2/\lambda^2} \tag{1}$$

with $\mathbf{r} = |\mathbf{x}'' - \mathbf{x}'|$ denoting the lag distance.

Our study neglects the effects of density variations. This assumption is reasonable when dealing with 2D planar flow fields and for solutes characterized by density values similar to the surrounding fluid. Regarding the latter, the densities of certain contaminants are similar to water. Examples consist of m-cresol, chlorobenzene, and benzene (with densities equal to 1.03, 1.11, and 0.88 g/ml respectively).

For our work, we designate dimensional variables with the hat symbol ($\hat{\cdot}$). The governing equation for the flow field is thus given by

$$c_t \frac{\partial \hat{p}(\hat{\mathbf{x}}, \hat{t})}{\partial \hat{t}} + \nabla_{\hat{\mathbf{x}}} \cdot \hat{\mathbf{q}}(\hat{\mathbf{x}}, \hat{t}) = 0, \tag{2}$$

where $\hat{\mathbf{q}}$ is the specific discharge, $\hat{p}$ denotes the pore fluid pressure and c_t represents compressibility. Assuming incompressible flow ($c_t \approx 0$) in the absence of both sinks/sources and temporally variable boundary conditions, Eq. (2) becomes

$$\nabla_{\hat{\mathbf{x}}} \cdot \hat{\mathbf{q}}(\hat{\mathbf{x}}, \hat{t}) = 0. \tag{3}$$

The heterogeneous permeability field is mapped on the specific discharge through Darcy's law:

$$\hat{\mathbf{q}}(\hat{\mathbf{x}}, \hat{t}) = -\frac{\hat{k}(\hat{\mathbf{x}})}{\hat{\mu}(\hat{C}(\hat{\mathbf{x}}, \hat{t}))} \nabla_{\hat{\mathbf{x}}} \hat{p}(\hat{\mathbf{x}}, \hat{t}), \tag{4}$$

where $\hat{\mu}$ is the ambient fluid mixture's viscosity, which depends on the concentration $\hat{C}$ of the injected solute, and $\hat{p}$ denotes the pore fluid pressure. In this work we consider that the fluid carrying the solute has a viscosity different than the viscosity of the ambient fluid and we assume an exponential viscosity model [20]:

$$\hat{\mu}(\hat{C}(\hat{\mathbf{x}}, \hat{t})) = \mu_0 e^{-R\frac{\hat{C}(\hat{\mathbf{x}}, \hat{t})}{C_o}} \tag{5}$$

and R is the log-viscosity ratio, $R = \ln[\mu_0/\mu_1]$, C_o is the inlet concentration of the solute, μ_0 is the viscosity of the pure fluid in the absence of a solute, and μ_1 is the viscosity of the solute. We consider permeameter-like boundary conditions, i.e., prescribed pressures at the inlet ($x_1 = 0$) and outlet ($x_1 = L_1$) of the flow domain and zero flux at the layer boundaries $x_2 = 0$ and $x_2 = L_2$. Under these conditions, the spatially heterogeneous flow field is driven by uniform-in-the-mean pressure gradient.

An inert solute is instantaneously injected through an areal source zone with dimensions ℓ_1 and ℓ_2 (with $\ell_1 \ll \ell_2$) into the divergence-free Darcy flow. The spatiotemporal distribution of the solute concentration is provided by the advection-dispersion equation:

$$\phi \frac{\partial \hat{C}(\hat{\mathbf{x}}, \hat{t})}{\partial \hat{t}} + \hat{\mathbf{q}}(\hat{\mathbf{x}}, \hat{t}) \cdot \nabla_{\hat{\mathbf{x}}} \hat{C}(\hat{\mathbf{x}}, \hat{t}) = \phi D \nabla_{\hat{\mathbf{x}}}^2 \hat{C}(\hat{\mathbf{x}}, \hat{t}), \tag{6}$$

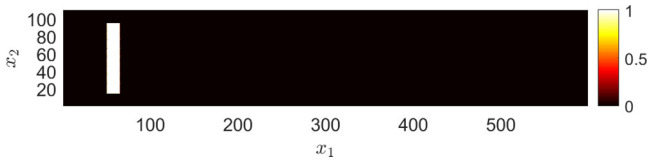

FIG. 1. Initial distribution of the concentration field in the flow domain. The solute is instantaneously injected along a rectangular source zone in a spatially heterogeneous porous medium.

where D corresponds to the local-scale dispersion coefficient (assumed to be constant) and is modelled through Scheidegger's theory [58]. The boundary conditions for the transport problem are periodic on the left and right boundaries, as well as the top and bottom of the domain. The initial condition for the concentration distribution, as reported in Fig. 1, is a zero concentration in the whole domain with the exception of the source area, where the concentration is set to be equal to unit value, with a small numerical perturbation on the edges to allow the formation of viscous fingers.

The Appendix reports the governing equations, i.e., Eqs. (3)–(6), in dimensionless form; see Eqs. (A2)–(A5). As indicated in the Appendix, the $\hat{}$ symbol is removed to denote all dimensionless variables [see dimensionless groups, Eq. (A1) in the Appendix]. The Appendix also shows that the dimensionless advection-dispersion equation is expressed in terms of the Péclet number. The Péclet number is given by $\mathrm{Pe} \equiv U\lambda/D$. Due to the dependence of $\mathbf{q}$ on the concentration field C, Eq. (A5) is nonlinear and needs to be solved numerically.

B. Mixing descriptors

The degree and rate of mixing can be quantified in the terms of the concentration variance (σ_c^2). The temporal evolution of σ_c^2 under periodic boundary conditions (or in absence of any net injection or extraction of the fluids) is governed by an ordinary differential equation that relates σ_c^2 to the mean scalar dissipation rate ϵ_c [20,59],

$$\frac{d\sigma_c^2(t)}{dt} = -2\epsilon_c(t). \tag{7}$$

The mean scalar dissipation rate is defined in terms of concentration gradients as

$$\epsilon_c(t) \equiv \frac{\langle |\nabla C(\mathbf{x}, t)|^2 \rangle}{\mathrm{Pe}}, \tag{8}$$

where $\langle \cdot \rangle$ denotes the spatial averaging operator.

III. ANALYSIS ON THE SOURCES OF DISORDER IN THE FLOW FIELD

A. Viscosity contrast and heterogeneity effects on vorticity

The viscosity contrast R and spatial heterogeneity in the k field induce fluctuations in the flow field, which give rise to fingering and channeling patterns on the solute interface. These fluctuations can be quantified in terms of the vorticity $\boldsymbol{\omega} = \nabla \times \mathbf{q}$ of the flow field. Using Eq. (4) and $\mu = e^{-\mathrm{RC}}$, we obtain [60]

$$\boldsymbol{\omega}(\mathbf{x}, t) = R\nabla C(\mathbf{x}, t) \times \mathbf{q}(\mathbf{x}, t) + \frac{1}{k(\mathbf{x})}\nabla k(\mathbf{x}) \times \mathbf{q}(\mathbf{x}, t) = \boldsymbol{\omega}_R(\mathbf{x}, t) + \boldsymbol{\omega}_k(\mathbf{x}, t), \tag{9}$$

which clearly shows how the two sources of disorder—viscosity contrast and heterogeneity—act on the flow field to generate two types of vorticity, $\boldsymbol{\omega}_R$ and $\boldsymbol{\omega}_k$, defined as $\boldsymbol{\omega}_R = R\nabla C(\mathbf{x}, t) \times \mathbf{q}(\mathbf{x}, t)$ and $\boldsymbol{\omega}_k = \frac{1}{k(\mathbf{x})}\nabla k(\mathbf{x}) \times \mathbf{q}(\mathbf{x}, t)$. In a 2D field, only the out-of-plane component of the vorticity vector is nonzero, i.e., $\boldsymbol{\omega} = [0, 0, \omega]$. Then Eq. (9) can be written in terms of the stream function ψ, which

is defined as $\partial\psi/\partial x_1 = -q_{x_2}$ and $\partial\psi/\partial x_2 = q_{x_1}$, to obtain

$$\omega(\mathbf{x},t) = -R\nabla C(\mathbf{x},t)\cdot\nabla\psi(\mathbf{x},t) - \nabla\ln[k(\mathbf{x})]\cdot\nabla\psi(\mathbf{x},t) = [\vartheta_R(\mathbf{x},t) + \vartheta_k(\mathbf{x})]\cdot\nabla\psi(\mathbf{x},t), \quad (10)$$

where we split the vorticity generation mechanisms into its two parts, ϑ_R and ϑ_k. The stream function and vorticity are also related to each other as $\nabla^2\psi = -\omega$.

Let us analyze the two sources individually.

(1) The magnitude of

$$\vartheta_R(\mathbf{x},t) = -R\nabla C(\mathbf{x},t) \quad (11)$$

increases with nonzero R and ∇C, the latter being a dynamic quantity. The interface between the initial solute cloud and the ambient fluid provides the initial ∇C, which is amplified by R to generate the vorticity near the interface that creates viscous fingers and further growth of the concentration gradients. This shows how the fingering process can grow like an instability. The concentration gradient initially sparks the creation of a finger, and the tip of the finger in turn "pushes" to travel faster than the ambient fluid, thus leading to the existence of a concentration gradient on the front of the interface between scalar and fluid; as the finger moves and progresses, such gradient moves along with it in the domain, causing local growth of the concentration gradient. Such local growth can be seen in more detail in Fig. 2.

(2) The magnitude of

$$\vartheta_k(\mathbf{x}) = -\nabla f(\mathbf{x}) \quad (12)$$

(with $f = \ln k$) is not, on the other hand, a dynamic quantity and is constant in time for a given permeability field.

These differences between the two sources of disorder, namely R and σ_f^2, give rise to different flow structures depending on whether viscosity contrast or heterogeneity dominates the flow (see Fig. 3). When fingering dominates heterogeneity (sufficiently large R compared to σ_f^2), vorticity ω_R is high immediately behind the sharp interface of a finger tip, which grows and becomes "rounder" as time increases until the tip splits into two nascent fingers [21,61]. Roundness and tip splitting of fingers is absent at $R = 0$ regardless of how high σ_f^2 is. Instead, fingers at high σ_f^2 gradually thins towards the tip and the tip fades away in analogy with the Taylor dispersion [62] effect (Fig. 3). In viscous fingering-dominated flow, Taylor dispersion at the tip is suppressed due to the vorticity from ϑ_R. This suppression happens because the solute cloud that is creating the finger has the tendency to travel fast, pushing against the front and keeping it sharp.

In this study, we consider both $R > 0$ and $R < 0$ displacements. Fingering occurs at the leading edge of the solute cloud in case of former and at the trailing edge in case of latter. For $R < 0$, the fingers are developed in the trailing edge of the plume, opposite to the direction of mean flow because their tips lie at the rear front of the less viscous fluid. The sign of R affects the viscosity contrast-induced vorticity, $\omega_R = -R\nabla C\cdot\nabla\psi$, in three important ways. The first effect is obvious because R appears explicitly in the expression of ω_R. The second effect is through the ∇C vector. Note that ω_R is nonzero only near the interface because ∇C is zero away from the interface. The direction of the ∇C vector changes along the entire interface and in particular along the interface of a single finger, which can be split into three regions: the curved tip, curved rear, and straight wall regions of the finger, as shown in Fig. 4. At the tip, ∇C and $\mathbf{q}$ vectors are opposite to each other for $R > 0$, whereas they point in the same direction for $R < 0$. The third effect is through the magnitude of $\mathbf{q}$. The transverse velocity q_{x_2} is highest near the tip and lowest along the wall region [63]. Moreover, q_{x_1} and q_{x_2} magnitudes are higher at the tip of an $R > 0$ finger than at the tip of an $R < 0$ finger, as is visible in Fig. 5.

B. Fingering mechanisms at $R \neq 0$

To understand the effect of fingering on the transport metrics of the solute cloud, we need to refer to the physical mechanisms of tip splitting, channeling, shielding, and merging of fingers that

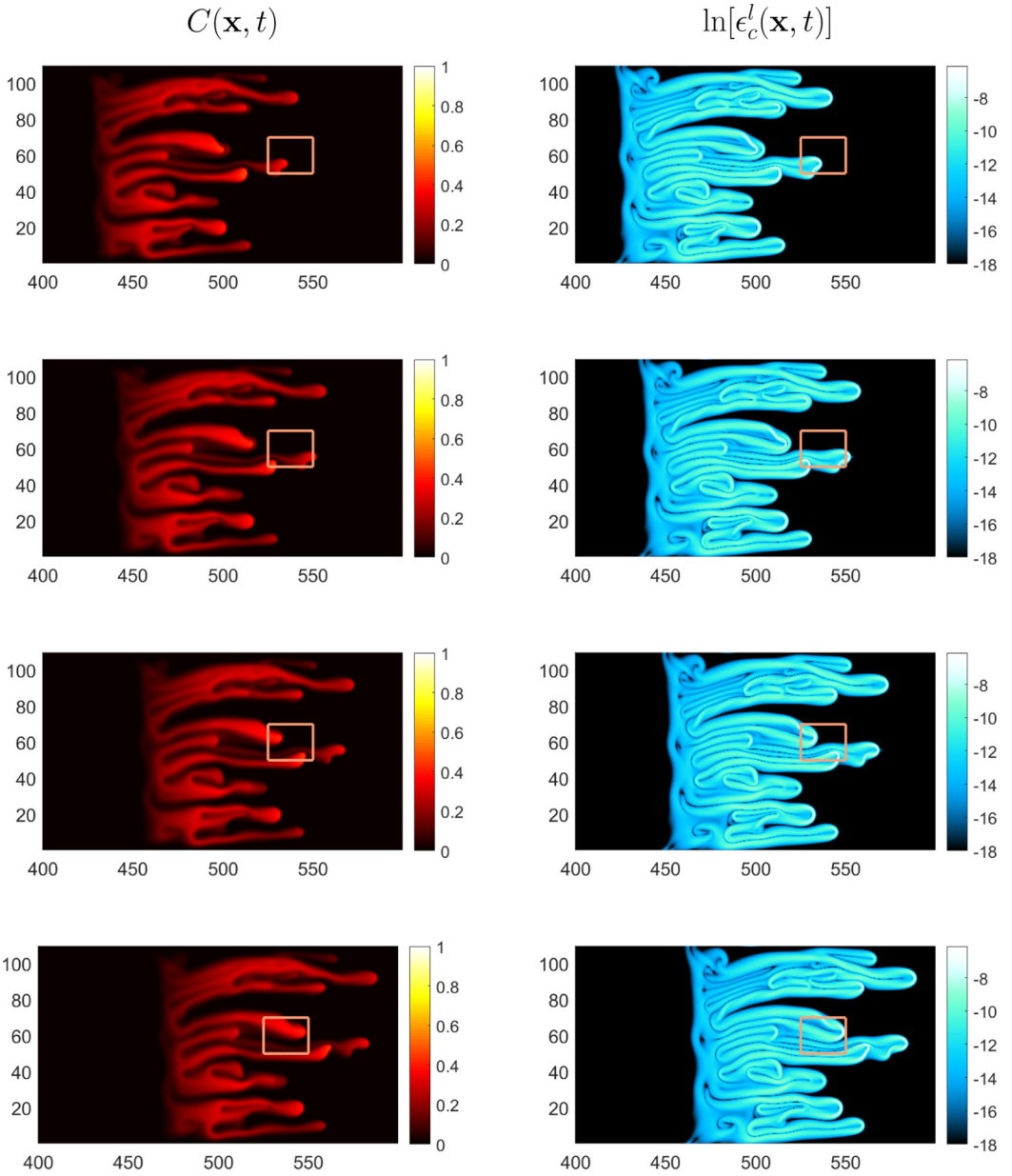

FIG. 2. Concentration field $C(\mathbf{x},t)$ (left column) and logarithm of the local scalar dissipation rate $\epsilon_c^l = \frac{|\nabla C(\mathbf{x},t)|^2}{\mathrm{Pe}}$ (right column) at four subsequent time steps (from top to bottom) for a viscosity contrast $R = 1$ in a homogeneous permeability field. Note how the concentration gradient progresses in the orange square, moving from the bottom left quadrant to occupy the whole bottom half in the first two time snapshots. As another finger enters the region defined by the orange square, the concentration gradient locally increases also in the upper half of the considered square.

have been observed in viscous fingering simulations and experiments; see, e.g., [21,23,36,41,61]. As mentioned above, tip splitting refers to the splitting of the tip of a finger into two smaller, nascent fingers. The nascent fingers compete with each other as well as with other fingers in their vicinity

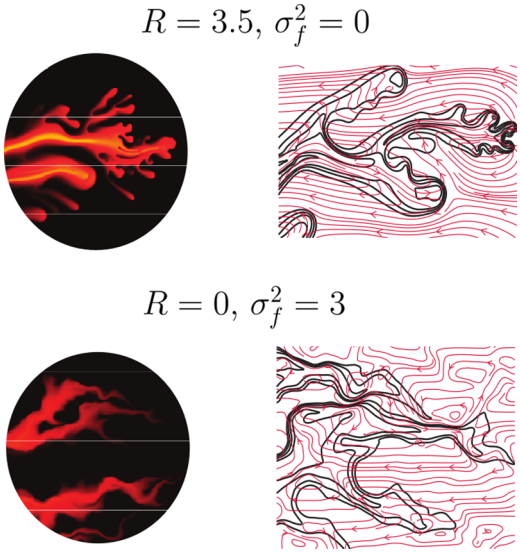

FIG. 3. Difference in the finger tip structures between fingering-dominated (*top row*) and heterogeneity-dominated (*bottom row*) flows. The left column shows the concentration fields in the two cases within a zoom-in view window. The right column shows the concentration contours (*black lines*) superposed on the streamlines (*red lines*). Fingering-dominated flows produce rounder and better delineated tips than heterogeneity-dominated flows. Fingering also produces tip splitting that is absent at $R = 0$.

by virtue of the global nature of the pressure field. This manifests as shielding of a smaller finger by a larger, faster-moving finger and merging of the smaller finger into the larger finger. The shielded finger experiences a stunted growth and either merges with the larger finger or fades away through diffusion. At high R, multiple merging and shielding events can lead to emergence of a single finger as a dominant feature of the flow. This is called channeling, which is often undesirable in mixing applications because it leads to a reduction in transverse mixing of the two fluids compared to the scenario where multiple fingers grow on the interface. However, note that channeling also implies a faster breakthrough at pumping wells which may be desirable during some contaminant removal operations. These fingering mechanisms are nonlinear and arise due to two-way coupling between

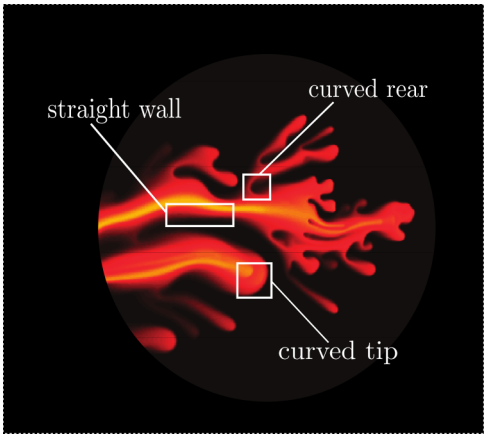

FIG. 4. Single finger regions: straight wall, curved rear, and curved tip.

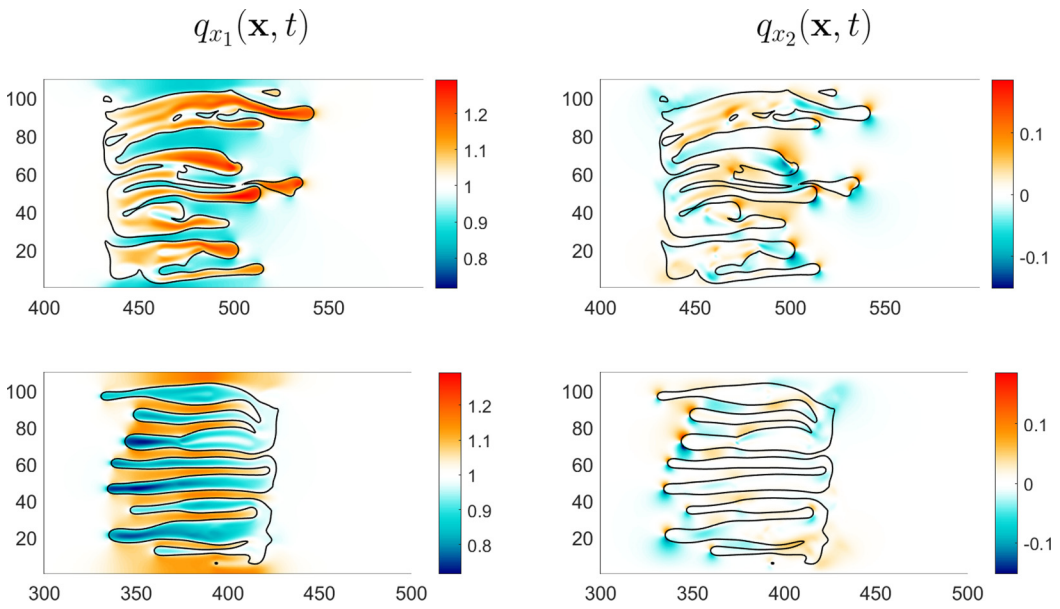

FIG. 5. Longitudinal and transversal velocity fields [$q_{x_1}(\mathbf{x}, t)$ and $q_{x_2}(\mathbf{x}, t)$ respectively] for a solute cloud with viscosity contrast $R = 1$ (top row) and $R = -1$ (bottom row) in a homogeneous field. The black lines represent the contour of the solute cloud at a threshold concentration value $C = 0.1$.

flow and transport processes. They remain active throughout the displacement period, albeit with different strengths. For example, tip splitting is more pronounced at early times whereas channeling emerges at later times. Also, the effect of two mechanisms can negate each other, e.g., tip splitting can negate merging in terms of their net effect on the interface length.

To understand the impact of the sign of R on the solute transport behavior, we can analyze how tip splitting and channeling mechanisms manifest themselves at the leading and trailing edges of the cloud. From Eq. (10), ω_R is larger at larger specific discharges q_{x_1} and q_{x_2}. Therefore, we expect tip splitting to be more pronounced at $R > 0$ than at $R < 0$ because the velocities q_{x_1} and q_{x_2} at the tip are higher at $R > 0$ than at $R < 0$. Channeling is almost exclusively reserved for $R > 0$ flows because the tip velocity (with respect to the mean flow velocity) is smaller in $R < 0$ than in $R > 0$.

IV. NUMERICAL MODEL AND IMPLEMENTATION

We use a second-order accurate finite volume method to solve Eq. (3) for cell-centered pressures. We linearize the equation by using the two-point flux approximation [64] of the Darcy flux in Eq. (4), which expresses the face-centered flux in terms of cell-centered pressures of the two neighboring cells and the face transmissibility computed from the harmonic mean of the cell permeabilities, viscosities, and dimensions. To solve the transport problem [Eq. (6)], we use a spectral method to discretize the spatial derivatives of cell-centered concentrations and a third-order explicit Runge-Kutta scheme to integrate time; see Refs. [20,41] for details. Higher-order accuracy of the spectral method allows us to resolve sharp gradients in the concentration field that arise from viscous fingering. The pressure field is relatively smooth because of the assumption of miscibility of the two fluids and, therefore, a second-order finite volume method provides sufficient numerical accuracy for the flow problem.

We use a 2D Cartesian grid with a uniform mesh size. Each grid block has dimensions $\Delta \times \Delta$ (see Table I). The number of cells is $N_x \times N_y = 1440 \times 264$ such that the ratio $\Delta/\lambda = 0.084$, in order to capture the effects of the spatially heterogeneous permeability field on the

TABLE I. Input parameters used in the simulations

Parameter	Symbol	Value	Calculated as
Correlation length in the x and y directions	λ	5 m	
Domain length in the x_1 direction	L_1	600 m	120λ
Domain length in the x_2 direction	L_2	110 m	22λ
Mesh size in the x_1 and x_2 directions	Δ	0.42 m	$\lambda/12$
Distance of source from top and bottom boundary	s_{tb}	15 m	3λ
Distance of source from left boundary	s_l	50 m	10λ
Length of source in the x_1 direction	ℓ_1	15 m	3λ
Length of source in the x_2 direction	ℓ_2	80 m	16λ
Longitudinal distance of control plane from left boundary	L_{cp}	250 m	50λ
Mean longitudinal flow velocity	U	1 m/d	
Local dispersivity	α	0.042 m^2	0.1Δ
Local scale dispersion coefficient	D	0.042 m^2/d	αU
Péclet number	Pe	120	$U\lambda/D$
Concentration at the source zone	C_o	1 mg/l	
Threshold concentration for solute cloud delineation	C^t	10^{-3} mg/l	

spatiotemporal dynamics of the solute cloud; see, e.g., [65–67]. The simulations were performed on high-performance computing nodes. Details about the input parameters for the numerical model are reported in Table I.

V. RESULTS

All computational results are reported in dimensionless form. Both longitudinal and transverse directions are normalized by λ, time is normalized by the advective timescale $\tau_u = \lambda/U$, and the concentration is normalized by the inlet concentration C_o.

In Fig. 6 we report the results of the simulations performed for a k field characterized by $\sigma_f^2 = 0.5$ at different times for the three selected values of viscosity contrast $R = -1$, 0, and 1. Qualitative analysis of Fig. 6 illustrates that the mixing behavior is different for different R values, for example the absence of viscosity contrast ($R = 0$) reduces the degree of mixing of the cloud. The exact quantification of this behavior is reported in the following sections. It is also clear that in the case of a positive R the solute cloud travels faster, while the opposite happens for negative values of R. This holds true also for the fields with $\sigma_f^2 = 0$ and $\sigma_f^2 = 0.25$ (not shown in Fig. 6). We can thus expect earlier first arrival times for cases where $R > 0$ with respect to transport in the absence of viscosity contrast. Figure 6 also shows that clouds with $R < 0$ will be characterized by late arrival times. This becomes clear in Fig. 7, which illustrates the impact of the mobility ratio R on the concentration breakthrough curve (BTC) at the control plane for different levels of heterogeneity. Note that Fig. 7 reports the averaged normalized concentration over the control plane (i.e., transverse direction) located at $x_1 = L_{cp}$, namely

$$\langle C(L_{cp}, x_2, t)\rangle_\perp = \frac{1}{L_2}\int_0^{L_2} C(L_{cp}, x_2, t)dx_2. \tag{13}$$

The case for a homogeneous porous media is illustrated in Fig. 7(a). As the level of heterogeneity increases, the maximum concentration decreases and macroscale spreading is augmented leading to more tailing effects [compare Figs. 7(a)–7(c)]. The effects of the mobility ratio are also clearly depicted in Fig. 7. For $R = 1$, the presence of fingering is pronounced in the leading edge of the solute cloud which leads to earlier breakthrough at the control plane as opposed to the case of $R = -1$. The asymmetry of the concentration signal at the control plane is amplified when R is

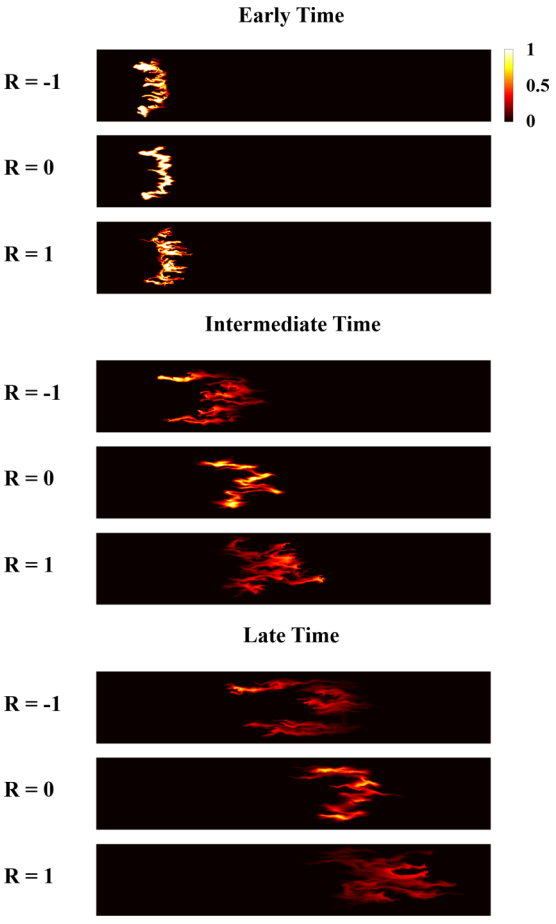

FIG. 6. Two-dimensional representation of the concentration distribution with k field characterized by $\sigma_f^2 = 0.5$ for three different values of viscosity ratio R at three different simulation times.

different than zero. On one hand, the effects of heterogeneity tend to diminish the impact of the mobility ratio on the maximum concentration [compare Fig. 7(b) with 7(c), results for $R = -1$ and $R = 1$). On the other hand, Fig. 7 clearly illustrates that the mobility ratio impacts the spreading of the solute cloud independent of the log-permeability variance. In all cases, the macrospreading effects [1] (the plume spreading induced by fluctuations in the sources of disorder) are larger for $R < 0$.

To evaluate the coupled effect of viscosity contrast and heterogeneity on early arrival times, we define the variable η as

$$\eta = \frac{t_e|_{R\neq 0}}{t_e|_{R=0}}, \tag{14}$$

where t_e is the time at which the normalized concentration reaches a value of $C = 0.05$. The trend of η for varying σ_f^2 is reported in Fig. 8, where the blue curve represents the cases with negative viscosity contrast while the light blue the positive one. From Fig. 8 is possible to notice that fingers in the front of the cloud travel faster with increasing levels of heterogeneity. The opposite occurs when fingers are developed in the tailing edge of the plume (i.e., the cloud slows down with respect to the case with $R = 0$). This means that the hydraulic connectivity (i.e., early arrival times) of the leading edge of the plume is enhanced for $R > 0$ whereas it is diminished for $R \leqslant 0$. These results

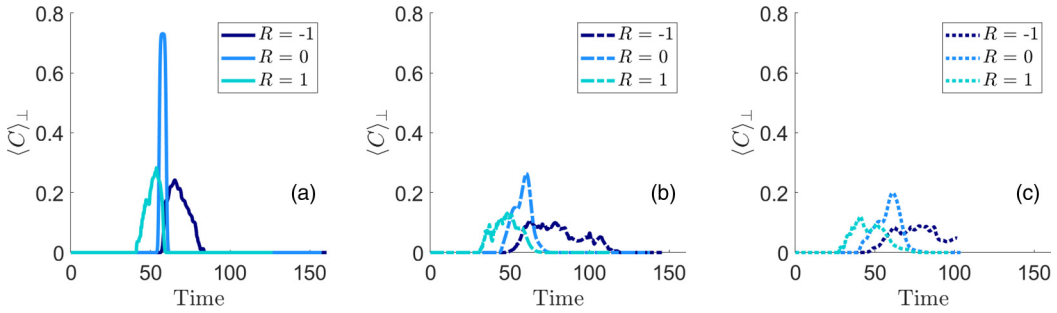

FIG. 7. Breakthrough curves (BTCs) at a control plane located at $x_1 = L_{cp}$ for the three different levels of heterogeneity of the permeability field: (a) homogeneous, (b) heterogeneous with $\sigma_f^2 = 0.25$, and (c) heterogeneous with $\sigma_f^2 = 0.5$.

show that neglecting viscosity contrast in transport models can have an impact on the estimation of early arrival times which are critical in risk analysis and contaminant site management; see, e.g., [12,68].

Next, we evaluate the spatial mean of the concentration (normalized by C_o) at all time steps (Fig. 9). The spatial mean is calculated in the region of the domain occupied by the solute cloud, defined as the volume $V(t)$ where the concentration is higher than the threshold value reported in Table I, $C(\mathbf{x}, t) > C^t$. The dimensionless mean concentration $\langle C \rangle$ is thus calculated as

$$\langle C \rangle = \frac{1}{V(t)} \int_{V(t)} C(\mathbf{x}, t) dV. \tag{15}$$

As shown in Fig. 9(a), for a homogeneous porous media the temporal evolution of the mean concentration is the same for both $R = 1$ and $R = -1$. Furthermore, the mean concentrations for $R \neq 0$ cases are lower than the one obtained in the absence of viscous fingering ($R = 0$). When $R \neq 0$, the presence of fingering contributes to an increase of the surface area of the solute cloud with the surrounding ambient fluid, also called interface stretching. It also contributes to a higher

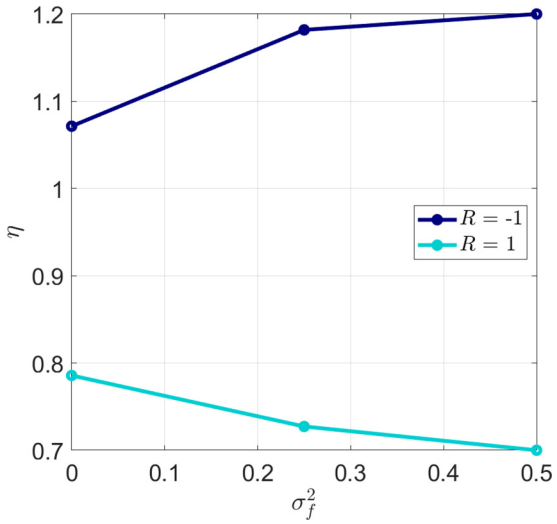

FIG. 8. Effect of the viscosity ratio R on η for increasing levels of heterogeneity of the permeability field. Results computed at $x_1 = L_{cp}$, where the value of L_{cp} is reported in Table I.

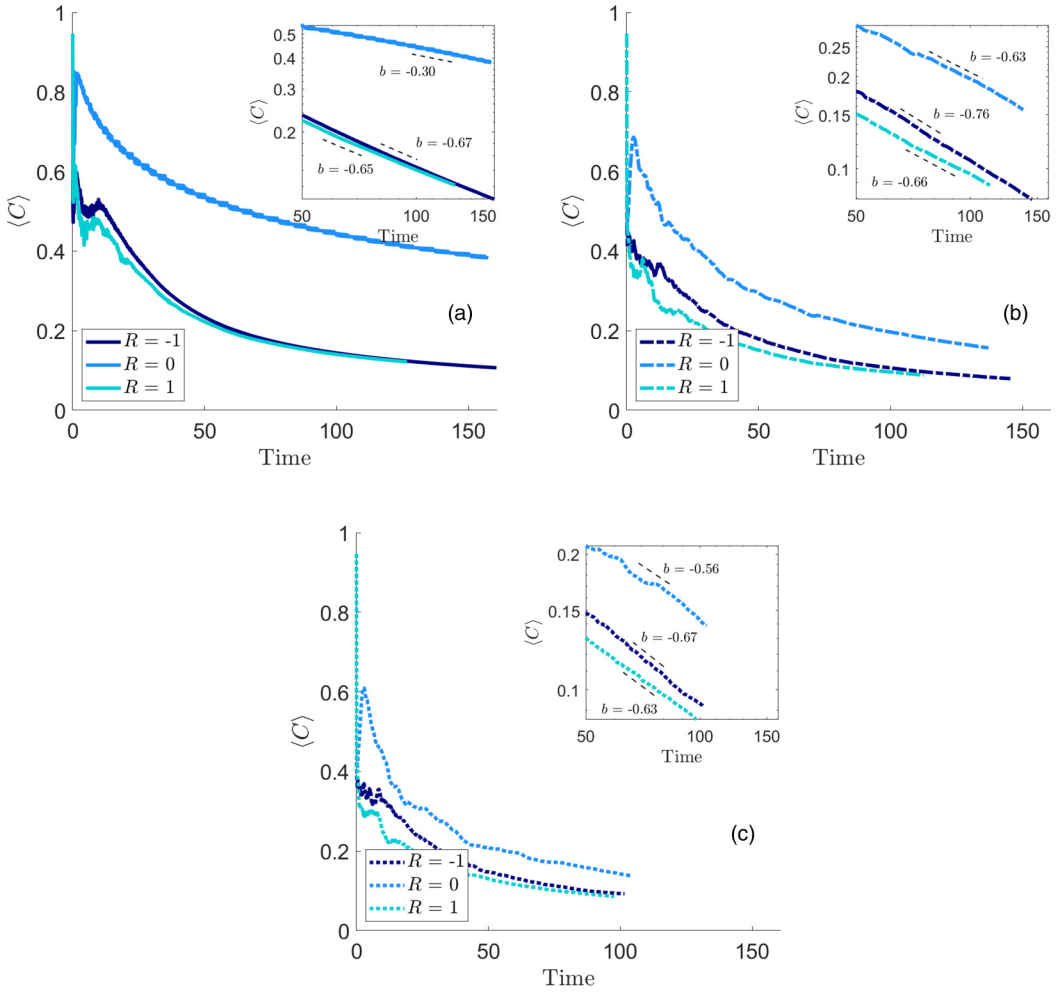

FIG. 9. Mean plume concentration for the three different levels of heterogeneity of the permeability field: (a) homogeneous, (b) heterogeneous with $\sigma_f^2 = 0.25$, and (c) heterogeneous with $\sigma_f^2 = 0.5$. In the insets the details of late times are plotted in a log-log scale, with the values of the parameter b.

concentration gradient along the interface. These two effects combined contribute to an enhancement of the diffusive mass flux across the interface, which in turn leads to a more diluted cloud. Furthermore, more vigorous tip splitting in the case of $R = 1$ increases the length of the fluid-fluid interface compared to $R = -1$, which explains the larger dilution or smaller mean concentration observed at $R = 1$. This explains also why, if we consider a scaling relation for the decay of the mean concentration $\langle C \rangle \sim t^b$ at large times, the values of b are always slightly higher in modulus for $R < 0$ than for $R > 0$. In fact, in the latter case the enhanced mixing at earlier times results into smaller magnitudes of the gradients at intermediate times which retards mixing at later times. Both cases however present a decay faster than the case of $R = 0$. The effects of the mobility ratio are reduced when the level of heterogeneity increases [compare Figs. 9(a)–9(c)].

Figure 10 depicts the temporal dynamics of the concentration variance (normalized by C_o^2) within the solute cloud of volume $V(t)$, calculated as

$$\sigma_c^2(t) = \frac{1}{V(t)} \int_{V(t)} [C(\mathbf{x}, t) - \langle C(t) \rangle]^2 dV. \tag{16}$$

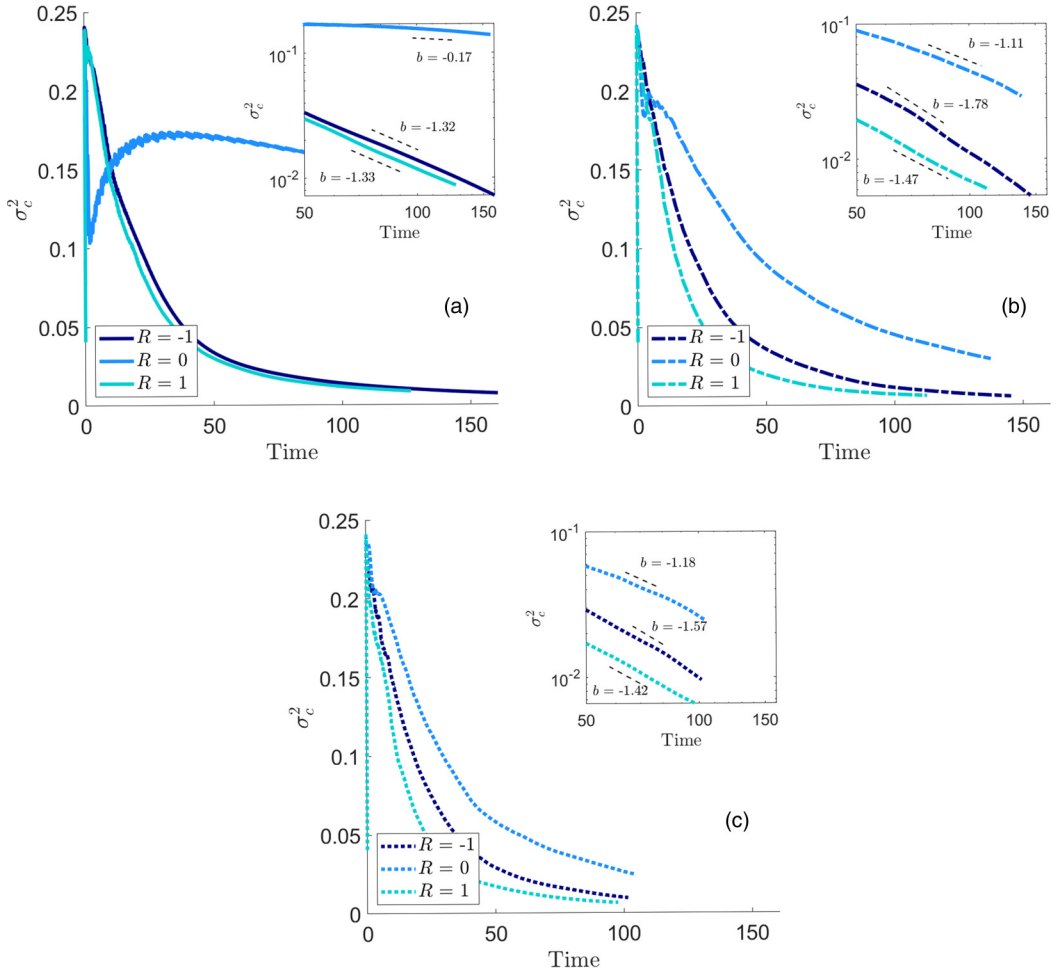

FIG. 10. Concentration variance of the solute cloud for the three different levels of heterogeneity of the permeability field: (a) homogeneous, (b) heterogeneous with $\sigma_f^2 = 0.25$, and (c) heterogeneous with $\sigma_f^2 = 0.5$.

As observed in Fig. 10, the presence of fingering causes a sudden increase of the concentration variance followed by fast decay when compared to the $R = 0$ case, regardless of the level of heterogeneity. Similarly to the mean concentration behavior observed in Fig. 9, more vigorous tip splitting in the case of $R > 0$ leads to an increase of the surface area of the solute body with the surrounding fluid which contributes to the dilution of the cloud and, therefore, lower variance [compare curves for $R = -1$ and $R = 1$ in Figs. 10(b) and 10(c)]. It is interesting to note the difference in the impact of R between the heterogeneous and homogeneous cases. In fact, for the heterogeneous cases, the curves for $R = -1$ and $R = 1$ become more distinct with respect to the homogeneous one.

The cumulative distribution function (CDF) of the concentration field is plotted at different times for $\sigma_f^2 = 0.5$ and $R = -1$, 0 and 1 in Fig. 11. As shown in Fig. 11, the probability that the concentration is below a certain value (i.e., $C = 0.25$) is higher for $R = 1$ [Fig. 11(c)] when compared to the case of $R = -1$ [Fig. 11(a)]. The tip-splitting mechanism, which is stronger for positive values of R, is the key reason for the increase in the likelihood of observing lower concentrations. As shown in the literature [69], the concavity of the CDF can be used as a measure

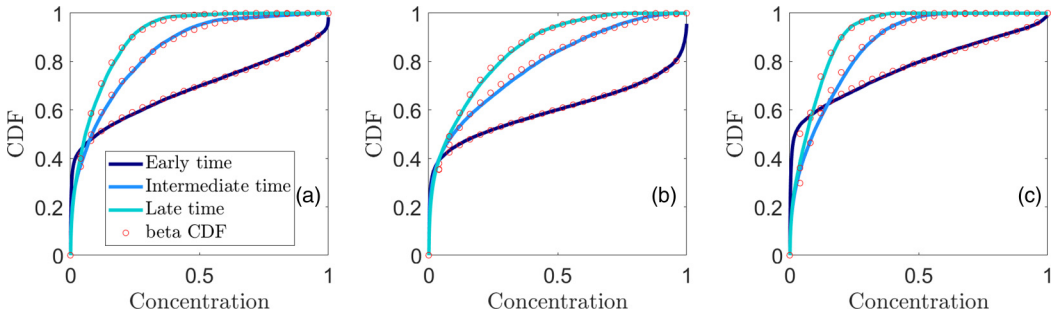

FIG. 11. Cumulative density function of the plume concentration in the k field with $\sigma_f^2 = 0.5$ at three different simulation times for three different values of viscosity ratio R: (a) $R = -1$, (b) $R = 0$, and (c) $R = 1$.

of the dilution state of the solute body. Based on the evidence published in previous papers in the turbulence, atmospheric and hydrologic communities [54,70–72], the concentration CDF can be approximated by a beta distribution for transport in spatially variable flow fields. Here we examine if the beta distribution can approximate the concentration distribution in the presence of viscous fingering. The beta CDF is given by

$$\mathcal{P}_C(c;\mathbf{x},t) = \frac{\Gamma[a_o + b_o]}{\Gamma[a_o(\mathbf{x},t)]\Gamma[b_o(\mathbf{x},t)]} \int_0^c \chi^{a_o(\mathbf{x},t)-1}(1-\chi)^{b_o(\mathbf{x},t)-1} d\chi,$$

with

$$\begin{aligned} \Gamma[z] &= \int_0^\infty \zeta^{z-1} e^{-\zeta} d\zeta, \\ a_o(\mathbf{x},t) &= \frac{\langle C(\mathbf{x},t)\rangle}{\beta(\mathbf{x},t)}, \\ b_o(\mathbf{x},t) &= \frac{1-\langle C(\mathbf{x},t)\rangle}{\beta(\mathbf{x},t)}, \\ \beta(\mathbf{x},t) &= \frac{\sigma_c^2(\mathbf{x},t)}{\langle C(\mathbf{x},t)\rangle[1-\langle C(\mathbf{x},t)\rangle] - \sigma_c^2(\mathbf{x},t)}, \end{aligned} \tag{17}$$

where $\Gamma[z]$ is the gamma function.

Figure 11 depicts an excellent agreement between the empirical CDF (obtained from the raw numerical data) and the beta CDF model [Eq. (17)] parametrized by the mean and variance of C, namely $\langle C\rangle$ and σ_c^2. From an application point of view, both quantities, i.e., concentration mean and variance, can be estimated from monitoring wells in a contaminated site [54]. The results reported in Fig. 11 show that the beta-CDF model can be employed to capture the full probabilistic distribution of the solute cloud in the presence of viscous fingering for the range of heterogeneity and mobility ratio explored in this work, i.e., $\sigma_f^2 < 1$ and $-1 \leqslant R \leqslant 1$. This result can be used to predict the probability that the solute concentration will exceed a threshold value which is of importance in risk analysis and aquifer remediation [54,69].

The temporal evolution of the mean scalar dissipation rate [Eq. (8) is presented in Fig. 12 for the homogeneous and heterogeneous flows. As illustrated in Fig. 12, the presence of viscous fingering leads to a sharp increase in the scalar dissipation rate followed by a decay. The differences between the curves for $R = -1$, 0, and 1 are attenuated in the heterogeneous scenarios [compare Fig. 12(a) with Figs. 12(b) and 12(c)]. In all cases, the peak of the scalar dissipation rate is higher for $R = 1$.

Figure 13 illustrates the solute cloud's contour length evolution in time. The contour length is computed based on the normalized concentration $C^* = 0.05$ isoline. As shown in Fig. 13, the effect of the medium's disorder contributes to an increase of the cloud's contour length. For the

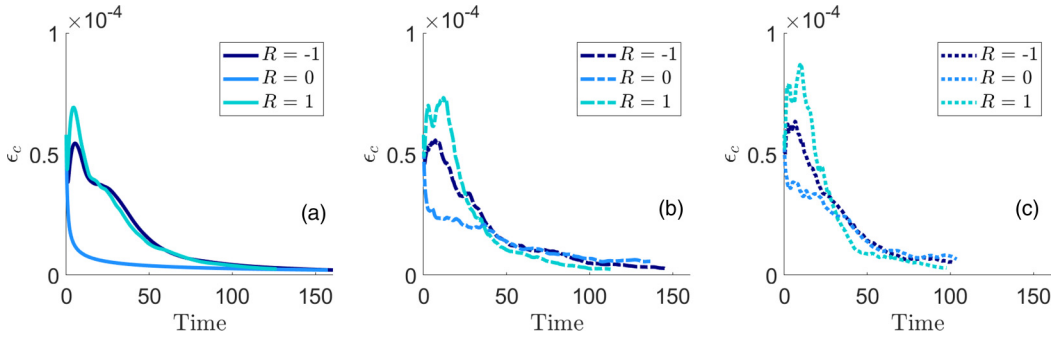

FIG. 12. Mean scalar dissipation rate ϵ_c for the three different levels of heterogeneity of the permeability field: (a) homogeneous, (b) heterogeneous with $\sigma_f^2 = 0.25$, and (c) heterogeneous with $\sigma_f^2 = 0.5$.

heterogeneous cases, i.e., $\sigma_f^2 = 0.25$ and 0.5, the contour length is larger for $R = 1$ than the ones computed for $R = -1$.

Next, we quantify the relative contribution of the medium's disorder level and the viscosity contrast on solute mixing. In order to do so, the effects of heterogeneity and viscosity contrast have been here quantified by normalizing the mean scalar dissipation rate ϵ_c (Fig. 12) to the cases where those effects are not present. The heterogeneity-induced dissipation is represented by the parameter ξ thus calculated as

$$\xi(t) = \frac{\epsilon_c(t|R, \sigma_f) - \epsilon_c(t|R, \sigma_f = 0)}{\epsilon_c(t|R, \sigma_f = 0)}, \tag{18}$$

while the finger-induced dissipation is quantified by φ as

$$\varphi(t) = \frac{\epsilon_c(t|R, \sigma_f) - \epsilon_c(t|R = 0, \sigma_f)}{\epsilon_c(t|R = 0, \sigma_f)}. \tag{19}$$

The temporal evolution of ξ and φ is reported in Fig. 14 for the cases where both heterogeneity and viscosity contrast are present. It is clear that at early times the effects induced by the viscosity contrast are more pronounced on the dissipation rate as opposed to the ones induced by the physical heterogeneity, as the values of φ in Fig. 14(a) are higher than the values of ξ in Fig. 14(b). From Fig. 14(a), we notice that for the same level of heterogeneity, a positive viscosity contrast has a greater impact on ϵ_c compared to a negative R case. At parity of R, the fingering effect on mixing is attenuated by higher levels of heterogeneity, which is as expected. At later times, on the other hand, heterogeneity [Fig. 14(b)] becomes the main contributor to dissipation, though its importance

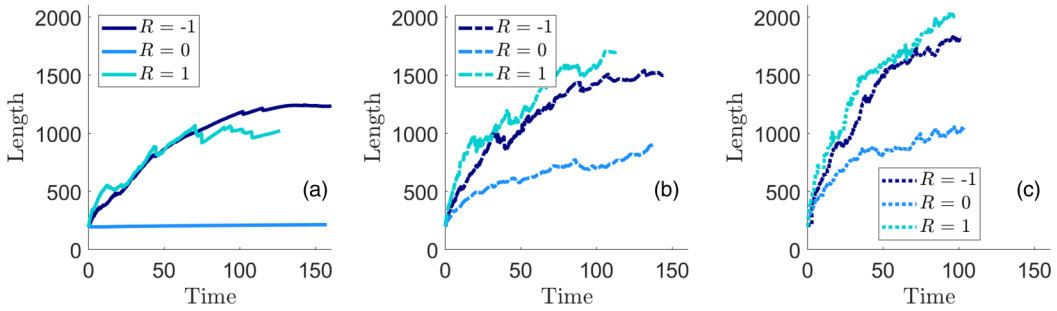

FIG. 13. Evolution of the length of $C = 0.05$ contour for the three different levels of heterogeneity of the permeability field: (a) homogeneous, (b) heterogeneous with $\sigma_f^2 = 0.25$, and (c) heterogeneous with $\sigma_f^2 = 0.5$.

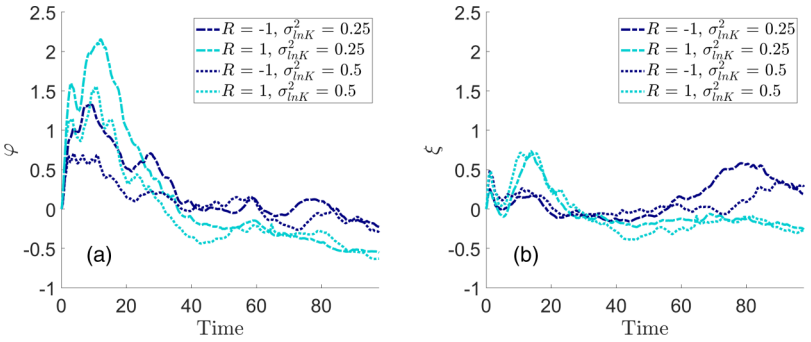

FIG. 14. Trends in time of the mean scalar dissipation rate ϵ_c normalized with respect to (a) the effect of viscosity contrast, defined by the metric φ [Eq. (19)] and to (b) the effect of heterogeneity, defined by the metric ξ [Eq. (18)].

is relatively marginal compared to the viscosity contribution to mixing at early times. The behavior of ξ at parity of R does not seem to be greatly affected by an increase in σ_f^2, but this may be due to the fact that the considered levels of heterogeneity do not differ much. However, heterogeneity seems to enhance mixing at later times especially for $R < 0$; this can be explained considering that mixing happens faster for $R > 0$, so at later times the process is almost over, while for $R < 0$ heterogeneity has sufficient time to kick in and have a more significant impact. This suggests that, for the simulations considered here, the timescale of fingering-induced mixing mechanism is shorter than that of the heterogeneity-induced mixing mechanism. The two time scales can further be related to the length scales of diffusion (Pe) and permeability correlation length (λ). The prescribed initial condition on the concentration field, i.e., the sharpness of the interface at $t = 0$, also affects the separation of two timescales in this plot [44].

VI. SUMMARY

In this paper we investigate the impact of two sources of disorder, namely viscous fingering and permeability heterogeneity, on the temporal evolution of key statistical descriptors of transport. Our numerical simulations indicate that at early times the viscosity contrast is the dominant source of disorder, and its impact on the arrival times at a control plane is enhanced by heterogeneity, while permeability heterogeneity decreases the values of peak concentration at a control plane and increases solute cloud spreading. In particular, we highlight the following points:

(1) Heterogeneity reduces the peak concentration observed at the control plane and, while it does not affect the impact of the viscosity ratio, it produces asymmetry in the BTCs and a larger cloud spreading for $R < 0$.

(2) A positive viscosity contrast enhances the connectivity of leading edge of the solute cloud which leads to earlier breakthrough, while a negative viscosity contrast delays the arrival of the solute to the control plane; this opposite impact of viscosity on connectivity increases with increasing levels of heterogeneity.

(3) At late times, the mean concentration decay is described by a relation of the type $\langle C \rangle \sim t^b$, where the effect of the mobility ratio on the value of b is reduced for higher level of heterogeneity.

(4) The concentration CDF, whose concavity can be used as a proxy for dilution [69], can be perfectly described as a beta distribution (parametrized solely by the concentration spatial mean and variance) in the presence of viscous fingering for the range of σ_f^2 and R considered in the present study. This result can be used for predictions in risk analysis, and to the authors' knowledge has never been shown before for flow in the presence of viscosity contrast.

(5) The mean scalar dissipation rate for $R \neq 0$ presents a sharp increase at early times, with higher peaks for $R > 0$ because of the more intense tip splitting.

(6) Longer cloud contours (and thus mixing interfaces) are caused by higher heterogeneity levels and viscosity contrast, with $R > 0$ having a bigger impact on the contour than $R < 0$.

(7) At early times the effect of viscosity contrast on mixing is more significant than the effect of heterogeneity, despite being attenuated for increasing values of σ_f^2. At later times, the impact of heterogeneity becomes the main contributor to mixing, especially for $R < 0$.

The results shown in this study illustrate the importance of viscous fingering and heterogeneity in controlling the temporal evolution of the statistical descriptors of the solute cloud. The conclusions reported in our work are limited to the range of values explored for σ_f^2 and R. Future research should investigate the effects of higher level of heterogeneity on mixing in the presence of viscous fingering as well as their relative contributions in three-dimensional flows.

ACKNOWLEDGEMENT

The authors acknowledge the support provided by the NSF Grant No. 2025285.

APPENDIX: DIMENSIONLESS EQUATIONS

We define the following dimensionless groups:

$$\mathbf{x} = \frac{\hat{\mathbf{x}}}{\lambda}, \quad \mathbf{u} = \frac{\hat{\mathbf{u}}}{U}, \quad \mathbf{t} = \frac{\hat{\mathbf{t}}}{\tau_u}, \quad C = \frac{\hat{C}}{C_o}, \quad \mu = \frac{\hat{\mu}}{\mu_0}, \quad p = \frac{\hat{p}}{p_c}, \quad k = \frac{\hat{k}}{k_c}, \tag{A1}$$

where the $(\hat{\cdot})$ symbol denotes a dimensional variable. Here λ represents the characteristic length scale (i.e., log-permeability correlation scale), U denotes the characteristic (mean longitudinal) velocity, and $\tau_u = \lambda/U$ corresponds to the characteristic advective timescale. The inlet concentration is C_o. Furthermore, we set the ambient fluid viscosity μ_0 as a characteristic viscosity and a unitary value for the characteristic permeability $k_c = 1\ \mathrm{m}^2$. Finally, the characteristic pressure is defined as $p_c = \mu_0 U\lambda/k_c$. Substituting the dimensionless groups (A1) into Eqs. (3)–(6), we obtain

$$\mathbf{q} = -\frac{k}{\mu}\nabla_{\mathbf{x}} p, \tag{A2}$$

$$\mu = e^{-\mathrm{RC}}, \tag{A3}$$

$$\nabla_{\mathbf{x}} \cdot \mathbf{q} = 0, \tag{A4}$$

and

$$\frac{\partial C}{\partial t} + \frac{\mathbf{q}}{\phi} \cdot \nabla_{\mathbf{x}} C = \frac{1}{\mathrm{Pe}} \nabla_{\mathbf{x}}^2 C, \tag{A5}$$

where the Péclet number is given by $\mathrm{Pe} \equiv U\lambda/D$ and ϕ is the porosity of the porous medium.

[1] G. Dagan, Solute transport in heterogeneous porous formations, J. Fluid Mech. **145**, 151 (1984).

[2] D. L. Koch and J. F. Brady, Anomalous diffusion in heterogeneous porous media, Phys. Fluids **31**, 965 (1988).

[3] M. Dentz and J. Carrera, Mixing and spreading in stratified flow, Phys. Fluids **19**, 017107 (2007).

[4] F. P. J. de Barros, M. Dentz, J. Koch, and W. Nowak, Flow topology and scalar mixing in spatially heterogeneous flow fields, Geophys. Res. Lett. **39** (2012).

[5] O. A. Cirpka, M. Rolle, G. Chiogna, F. P. J. de Barros, and W. Nowak, Stochastic evaluation of mixing-controlled steady-state plume lengths in two-dimensional heterogeneous domains, J. Contam. Hydrol. **138**, 22 (2012).

[6] M. Dentz and F. P. J. de Barros, Mixing-scale dependent dispersion for transport in heterogeneous flows, J. Fluid Mech. **777**, 178 (2015).

[7] Y. Ye, G. Chiogna, O. A. Cirpka, P. Grathwohl, and M. Rolle, Experimental investigation of transverse mixing in porous media under helical flow conditions, Phys. Rev. E **94**, 013113 (2016).
[8] V. Kapoor and P. K. Kitanidis, Concentration fluctuations and dilution in aquifers, Water Resour. Res. **34**, 1181 (1998).
[9] M. Sahimi, H. T. Davis, and L. Scriven, Dispersion in disordered porous media, Chem. Eng. Commun. **23**, 329 (1983).
[10] A. Tyukhova, M. Dentz, W. Kinzelbach, and M. Willmann, Mechanisms of anomalous dispersion in flow through heterogeneous porous media, Phys. Rev. Fluids **1**, 074002 (2016).
[11] C. B. Rizzo and F. P. J. de Barros, Minimum hydraulic resistance and least resistance path in heterogeneous porous media, Water Resour. Res. **53**, 8596 (2017).
[12] F. P. J. de Barros, S. Ezzedine, and Y. Rubin, Impact of hydrogeological data on measures of uncertainty, site characterization and environmental performance metrics, Adv. Water Resour. **36**, 51 (2012).
[13] F. P. J. de Barros, D. Fernàndez-Garcia, D. Bolster, and X. Sanchez-Vila, A risk-based probabilistic framework to estimate the endpoint of remediation: Concentration rebound by rate-limited mass transfer, Water Resour. Res. **49**, 1929 (2013).
[14] A. Hartmann, T. Gleeson, Y. Wada, and T. Wagener, Enhanced groundwater recharge rates and altered recharge sensitivity to climate variability through subsurface heterogeneity, Proc. Natl. Acad. Sci. USA **114**, 2842 (2017).
[15] R. M. Maxwell and W. E. Kastenberg, Stochastic environmental risk analysis: An integrated methodology for predicting cancer risk from contaminated groundwater, Stochastic Environ. Res. Risk Assess. **13**, 27 (1999).
[16] C. V. Henri, D. Fernàndez-Garcia, and F. P. J. de Barros, Assessing the joint impact of DNAPL source-zone behavior and degradation products on the probabilistic characterization of human health risk, Adv. Water Resour. **88**, 124 (2016).
[17] S. D. Hovorka, C. Doughty, S. M. Benson, K. Pruess, and P. R. Knox, The impact of geological heterogeneity on CO_2 storage in brine formations: A case study from the Texas Gulf Coast, Geol. Soc., London, Spec. Publ. **233**, 147 (2004).
[18] Z. Dai, Y. Zhang, J. Bielicki, M. A. Amooie, M. Zhang, C. Yang, Y. Zou, W. Ampomah, T. Xiao, W. Jia *et al.*, Heterogeneity-assisted carbon dioxide storage in marine sediments, Appl. Energy **225**, 876 (2018).
[19] C. Nicolaides, B. Jha, L. Cueto-Felgueroso, and R. Juanes, Impact of viscous fingering and permeability heterogeneity on fluid mixing in porous media, Water Resour. Res. **51**, 2634 (2015).
[20] B. Jha, L. Cueto-Felgueroso, and R. Juanes, Fluid Mixing from Viscous Fingering, Phys. Rev. Lett. **106**, 194502 (2011).
[21] G. M. Homsy, Viscous fingering in porous media, Annu. Rev. Fluid Mech. **19**, 271 (1987).
[22] P. G. Saffman, Viscous fingering in Hele-Shaw cells, J. Fluid Mech. **173**, 73 (1986).
[23] M. Tran and B. Jha, Coupling between transport and geomechanics affects spreading and mixing during viscous fingering in deformable aquifers, Adv. Water Resour. **136**, 103485 (2020).
[24] L. Van der Meer, The conditions limiting CO_2 storage in aquifers, Energy Convers. Manage. **34**, 959 (1993).
[25] B. S. Broyles, R. A. Shalliker, D. E. Cherrak, and G. Guiochon, Visualization of viscous fingering in chromatographic columns, J. Chromatogr., A **822**, 173 (1998).
[26] A. R. Kopf-Sill and G. Homsy, Nonlinear unstable viscous fingers in Hele-Shaw flows. I. Experiments, Phys. Fluids **31**, 242 (1988).
[27] P. Petitjeans, C.-Y. Chen, E. Meiburg, and T. Maxworthy, Miscible quarter five-spot displacements in a Hele-Shaw cell and the role of flow-induced dispersion, Phys. Fluids **11**, 1705 (1999).
[28] J.-C. Bacri, N. Rakotomalala, D. Salin, and R. Woumeni, Miscible viscous fingering: Experiments versus continuum approach, Phys. Fluids A **4**, 1611 (1992).
[29] R. J. Held and T. H. Illangasekare, Fingering of dense nonaqueous phase liquids in porous media: 1. Experimental investigation, Water Resour. Res. **31**, 1213 (1995).
[30] V. Kretz, P. Berest, J. Hulin, and D. Salin, An experimental study of the effects of density and viscosity contrasts on macrodispersion in porous media, Water Resour. Res. **39**, 1032 (2003).

[31] G. Davies *et al.*, Miscible displacements in a heterogeneous rock: Detailed measurements and accurate predictive simulation, in *SPE Annual Technical Conference and Exhibition* (Society of Petroleum Engineers, Richardson, TX, 1991).
[32] L. Kempers and H. Haas, The dispersion zone between fluids with different density and viscosity in a heterogeneous porous medium, J. Fluid Mech. **267**, 299 (1994).
[33] M. Christie *et al.*, High-resolution simulation of unstable flows in porous media, SPE Reservoir Eng. **4**, 297 (1989).
[34] B. Rubin *et al.*, Compositional reservoir simulation with a predictive model for viscous fingering, in *SPE Symposium on Reservoir Simulation* (Society of Petroleum Engineers, Richardson, TX, 1993).
[35] H. Tchelepi *et al.*, Interaction of viscous fingering, permeability heterogeneity, and gravity segregation in three dimensions, SPE Reservoir Eng. **9**, 266 (1994).
[36] C. T. Tan and G. M. Homsy, Simulation of nonlinear viscous fingering in miscible displacement, Phys. Fluids **31**, 1330 (1988).
[37] W. Zimmerman and G. Homsy, Three-dimensional viscous fingering: A numerical study, Phys. Fluids A **4**, 1901 (1992).
[38] A. De Wit, Y. Bertho, and M. Martin, Viscous fingering of miscible slices, Phys. Fluids **17**, 054114 (2005).
[39] M. Mishra, M. Martin, and A. De Wit, Differences in miscible viscous fingering of finite width slices with positive or negative log-mobility ratio, Phys. Rev. E **78**, 066306 (2008).
[40] C.-Y. Chen and E. Meiburg, Miscible porous media displacements in the quarter five-spot configuration. Part 2. Effect of heterogeneities, J. Fluid Mech. **371**, 269 (1998).
[41] B. Jha, L. Cueto-Felgueroso, and R. Juanes, Quantifying mixing in viscously unstable porous media flows, Phys. Rev. E **84**, 066312 (2011).
[42] B. Jha, L. Cueto-Felgueroso, and R. Juanes, Synergetic Fluid Mixing from Viscous Fingering and Alternating Injection, Phys. Rev. Lett. **111**, 144501 (2013).
[43] C. Welty and L. W. Gelhar, Stochastic analysis of the effects of fluid density and viscosity variability on macrodispersion in heterogeneous porous media, Water Resour. Res. **27**, 2061 (1991).
[44] C.-T. Tan and G. Homsy, Viscous fingering with permeability heterogeneity, Phys. Fluids A **4**, 1099 (1992).
[45] H. Tchelepi *et al.*, The interaction of viscous fingering, permeability heterogeneity and gravity segregation in 3D, in *SPE Symposium on Reservoir Simulation* (Society of Petroleum Engineers, Richardson, TX, 1993).
[46] D. Loggia, N. Rakotomalala, D. Salin, and Y. Yortsos, Phase diagram of stable miscible displacements in layered porous media, Europhys. Lett. **36**, 105 (1996).
[47] A. De Wit and G. Homsy, Viscous fingering in periodically heterogeneous porous media. I. Formulation and linear instability, J. Chem. Phys. **107**, 9609 (1997).
[48] A. De Wit and G. Homsy, Viscous fingering in periodically heterogeneous porous media. II. Numerical simulations, J. Chem. Phys. **107**, 9619 (1997).
[49] M. Sajjadi and J. Azaiez, Scaling and unified characterization of flow instabilities in layered heterogeneous porous media, Phys. Rev. E **88**, 033017 (2013).
[50] J. Nijjer, D. Hewitt, and J. Neufeld, Stable and unstable miscible displacements in layered porous media, J. Fluid Mech. **869**, 468 (2019).
[51] A. Libera, F. P. de Barros, and A. Guadagnini, Influence of pumping operational schedule on solute concentrations at a well in randomly heterogeneous aquifers, J. Hydrol. **546**, 490 (2017).
[52] T. Le Borgne, M. Dentz, and E. Villermaux, The lamellar description of mixing in porous media, J. Fluid Mech. **770**, 458 (2015).
[53] F. P. J. de Barros, A. Fiori, F. Boso, and A. Bellin, A theoretical framework for modeling dilution enhancement of non-reactive solutes in heterogeneous porous media, J. Contam. Hydrol. **175**, 72 (2015).
[54] F. Boso, F. P. J. de Barros, A. Fiori, and A. Bellin, Performance analysis of statistical spatial measures for contaminant plume characterization toward risk-based decision making, Water Resour. Res. **49**, 3119 (2013).
[55] P. Zhang, S. L. DeVries, A. Dathe, and A. C. Bagtzoglou, Enhanced mixing and plume containment in porous media under time-dependent oscillatory flow, Environ. Sci. Technol. **43**, 6283 (2009).

[56] M. Di Dato, F. P. J. de Barros, A. Fiori, and A. Bellin, Improving the efficiency of 3-D hydrogeological mixers: Dilution enhancement via coupled engineering-induced transient flows and spatial heterogeneity, Water Resour. Res. **54**, 2095 (2018).
[57] Y. Rubin, *Applied Stochastic Hydrogeology* (Oxford University Press, Oxford, 2003).
[58] A. E. Scheidegger, General theory of dispersion in porous media, J. Geophys. Res. **66**, 3273 (1961).
[59] T. Le Borgne, M. Dentz, D. Bolster, J. Carrera, J.-R. De Dreuzy, and P. Davy, Non-Fickian mixing: Temporal evolution of the scalar dissipation rate in heterogeneous porous media, Adv. Water Resour. **33**, 1468 (2010).
[60] M. Ruith and E. Meiburg, Miscible rectilinear displacements with gravity override. Part 2. Heterogeneous porous medium, J. Fluid Mech. **420**, 225 (2000).
[61] W. Zimmerman and G. Homsy, Nonlinear viscous fingering in miscible displacement with anisotropic dispersion, Phys. Fluids A **3**, 1859 (1991).
[62] G. I. Taylor, Dispersion of soluble matter in solvent flowing slowly through a tube, Proc. R. Soc. London, Ser. A: Math. Phys. Sci. **219**, 186 (1953).
[63] K. Ghesmat and J. Azaiez, Viscous fingering instability in porous media: Effect of anisotropic velocity-dependent dispersion tensor, Transp. Porous Media **73**, 297 (2008).
[64] R. J. LeVeque, *Finite Volume Methods for Hyperbolic Problems* (Cambridge University Press, Cambridge, UK, 2002).
[65] R. Ababou, D. McLaughlin, L. W. Gelhar, and A. F. Tompson, Numerical simulation of three-dimensional saturated flow in randomly heterogeneous porous media, Transp. Porous Media **4**, 549 (1989).
[66] A. Bellin, P. Salandin, and A. Rinaldo, Simulation of dispersion in heterogeneous porous formations: Statistics, first-order theories, convergence of computations, Water Resour. Res. **28**, 2211 (1992).
[67] Y. Rubin, A. Sun, R. Maxwell, and A. Bellin, The concept of block-effective macrodispersivity and a unified approach for grid-scale-and plume-scale-dependent transport, J. Fluid Mech. **395**, 161 (1999).
[68] F. P. J. de Barros, A. Bellin, V. Cvetkovic, G. Dagan, and A. Fiori, Aquifer heterogeneity controls on adverse human health effects and the concept of the hazard attenuation factor, Water Resour. Res. **52**, 5911 (2016).
[69] F. P. J. de Barros and A. Fiori, First-order based cumulative distribution function for solute concentration in heterogeneous aquifers: Theoretical analysis and implications for human health risk assessment, Water Resour. Res. **50**, 4018 (2014).
[70] C. Wall, B. J. Boersma, and P. Moin, An evaluation of the assumed beta probability density function subgrid-scale model for large eddy simulation of nonpremixed, turbulent combustion with heat release, Phys. Fluids **12**, 2522 (2000).
[71] R. Munro, P. Chatwin, and N. Mole, A concentration PDF for the relative dispersion of a contaminant plume in the atmosphere, Boundary Layer Meteorol. **106**, 411 (2003).
[72] A. Bellin and D. Tonina, Probability density function of non-reactive solute concentration in heterogeneous porous formations, J. Contam. Hydrol. **94**, 109 (2007).